Nanoscale Advances

Accepted Manuscript

This article can be cited before page numbers have been issued, to do this please use: A. Gupta and S. Ramasamy, *Nanoscale Adv.*, 2026, DOI: 10.1039/D6NA00397D.

ROYAL SOCIETY OF CHEMISTRY

rsc.li/nanoscale-advances

View Article Online
DOI: 10.1039/D6NA00397D

Unlocking the potential of p-block single-atom anchored on MXene electrocatalyst surface for efficient CO_2 reduction

Anshul Gupta[a,b] and Shanmugam Ramasamy[a]*

[a]Computational Insights and Sustainable Research Laboratory (CISRL),

CO_2 Research and Green Technologies Centre,

Vellore Institute of Technology, Vellore, Tamil Nadu 632014, India.

*shanmugam.r@vit.ac.in

[b]Department of Chemistry

School of Advanced Sciences (SAS), Vellore Institute of Technology, Vellore, Tamil Nadu 632014, India.

Abstract

The electrochemical reduction of CO_2 into value-added products has emerged as a promising approach for mitigating CO_2 emissions. In this study, 23 p-block single-atom (PSA)-anchored on Mo_2CO_2 catalyst for CO_2 reduction has been systematically investigated using density functional theory at atomic level. Based on the binding energy and cohesive energy, the 9 PSA prefers to anchor on Mo_2CO_2 hollow carbon site. Side-on and end-on modes are preferred for CO_2 adsorption on PSA-anchored Mo_2CO_2 (PSA@Mo_2CO_2). Projected density of states (PDOS) analysis indicates that PSA@Mo_2CO_2 exhibits a metallic-like electronic structure. The Bader charge analysis and charge density difference show unique behavior for Sn@Mo_2CO_2, with a lower Gibbs free energy change for the potential-determining step CO_2 to *OCHO (0.58 eV). Sn@Mo_2CO_2 is located on top of the volcano plot of limiting potential versus adsorption energy. Furthermore, Sn@Mo_2CO_2

View Article Online
DOI: 10.1039/D6NA00397D

exhibits the best selectivity for CO_2 reduction into HCOOH and suppresses the competing hydrogen evolution reaction. PDOS analysis of the *OCHO intermediate reveals that the oxygen and Sn p orbitals show moderate overlap. *Ab initio* molecular dynamics indicate that Sn@Mo_2CO_2 is stable at 300 K. This work provides an orbital-based strategy for catalyst design to enable selective CO_2 reduction to HCOOH.

Keywords: CO_2 electrochemical reduction, DFT studies, electrocatalyst, Single-atom catalyst, Mo_2CO_2, p-block

1. Introduction

In this technological and industrial era, energy consumption is increasing rapidly and continuously. Currently, the primary energy sources depend on fossil fuels. As a result, an enormous amount of CO_2 is continually being emitted into the atmosphere, which significantly contributes to global warming and has an adverse impact on the climate.[1] The Intergovernmental Panel on Climate Change (IPCC) has predicted that a 1.5 °C temperature rise or more is expected to occur within the next 20 years. CO_2 is inert and thermally stable due to its linear geometry and C=O bonds.[2] To address the above problems, identifying a suitable method for converting CO_2 into value-added products is essential. Among all approaches, the electrochemical reduction method using a sustainable catalyst offers several advantages, including operating at room temperature, using recyclable electrolytes, and integrating with renewable energy sources. Additionally, a more straightforward setup can be easily scaled to an industrial level.[3] Metal oxides, transition metal dichalcogenides, graphene, metal alloys, h-BN, metal-organic frameworks, and noble metal-based catalysts have been explored as potential electrocatalysts for CO_2 reduction.[4–10] However, all these processes still present numerous challenges, including high activation energy, sluggish kinetics, overpotential, and selectivity.[11,12]

View Article Online
DOI: 10.1039/D6NA00397D

Recently, single-atom catalysts (SAC) have garnered great interest due to their nearly 100% atom utilization efficiency, unique electronic properties, and low coordination of single atoms anchored on support material.[11,13] The SAC-based catalyst has shown better activity and performance as compared to that of their bulk counterpart in various reactions, such as oxygen evolution reaction (OER), oxygen reduction reaction (ORR)[14], nitrogen reduction reaction (NRR) [15], methane activation[16], hydrogen evolution reaction (HER)[17], and CO_2 reduction reaction (CRR).[18] Since the single atoms are highly unstable, suitable support materials are required to stabilize them and enhance their activity. Considering this, metal oxide[19], graphene[6], h-BN[20], transition metal dichalcogenide[21], phosphorene[22], and MXene[23] are explored as better support candidate materials.

Among all supports, MXene is currently the fastest growing 2D nanomaterial having the fascinating property and applications with the $M_{n+1}X_nT_x$ (n=1 to 3) general formula, where M is an early transition metal, X represents C or/N, and T_x represents the surface termination group, such as F, Cl, S, O, and OH. [24,25] MXene is a suitable support nanomaterial for single atoms due to its outstanding electrical conductivity, hydrophilicity, large surface area, and stability. The recently discovered MXene support is attracting attention for its exceptional properties.[26–28] Upon the strong interaction of a single atom with MXene, modified electronic states result, and an optimal active site for the intermediates' adsorption for better catalytic activity.[29–31] While considering suitable single atoms, researchers have mainly focused on transition-metal-based ones for a wide range of reactions due to their electron-accepting or donating properties toward adsorbates, arising from their partially filled d-orbitals.[23,25,32] In contrast, the p-block elements have filled d-orbitals and partially occupied p-orbitals, making them alternative candidates for a single-atom-based active site for the desired reactions.[31] However, few studies have been

View Article Online
DOI: 10.1039/D6NA00397D

performed on p-block single-atom (PSA) for HER and CRR. Zhang et al. [33] investigated the behavior of 14 non-metal-doped Mo_2CO_2 toward the HER reaction. In this work, surface oxygen gets activated by doping a non-metal in Mo_2CO_2. Calculated Gibbs free energies for hydrogen reveal that Cl (−0.06 eV), Br (−0.01 eV), and I (0.04 eV) doped Mo_2CO_2 show outstanding electrocatalytic activity towards HER. Ren et al. [21] designed a p-block (In, Bi, Pb, Sn, and Sb) metal-based single atom anchored on MoS_2 support for CO_2 reduction. Out of all PSA, Sb and Bi only show an excellent catalytic activity towards formic acid formation, with the limiting potential (U_L) value for Bi and Sb being −0.46 and −0.31V, respectively. Chen et al. [34] considered the single and double atom based on metals from the d and p-block elements on SnS_2, and it was found that the Sn-based single atom catalyst outperforms all the considered catalysts in the formation of formic acid. Guo et al. [31] constructed a SnN_4 single-atom active site with different secondary coordination sphere atoms, such as P, S, B, and N, for modulating the activity of the Sn single atom. Among all, Sn-N_3S_1 was found to improve the intermediate adsorption and activity. Liu et al.[35] reported that, among all PSA-doped Cu_2O, Ga-Cu_2O shows better catalytic performance for CRR. Because Ga makes a favourable interaction with the *OCHO intermediate for the formation of HCOOH. Hence, Cu_2O is also considered a suitable support for the PSA and has been explored for the CRR.

The SnS_2, MoS_2, and Cu_2O are semiconductors[36–38] whereas MXene-based support, Mo_2CO_2, is metallic in nature. [39] For a better electrocatalyst, metallic behavior is highly inevitable. The support Mo_2CO_2 is metallic, low-cost, and easy to synthesize, making it a viable catalyst in experiments.[39,40] Among MXene-based supports, Mo_2CO_2 has broad applications, including energy storage, electrocatalysis, and thermoelectric materials. [39–42] Hence, based on its properties, Mo_2CO_2 is considered a suitable support for PSA. Based on the literature, the Mo_2CO_2 MXene-

View Article Online
DOI: 10.1039/D6NA00397D

based support for the PSA catalyst has not been explored in greater detail for CRR. This research aims to explore the potential feasibility of a PSA on Mo_2CO_2 support for the electrocatalytic CRR to improve the stability, activity, and selectivity. In this work, we have systematically studied and analyzed the PSA on Mo_2CO_2 catalyst for CRR by using the density functional theory (DFT) approach.

2. Catalyst model and computational details

The Mo_2CO_2 modeled by a 3×3×1 supercell of Mo_2C (space group-$P6_3/mmc$) unit cell and surface-functionalized with oxygen atoms due to their stability, Mo_2CO_2 has a total number of 45 atoms (18 Mo, 9 C, and 18 O).[43,44] Cheng et al.[42] mention in their study that supercell 3×3×1 and 4×4×1 gave similar adsorption energy values for the adsorbate, which indicates that adsorption of the intermediate is not much affected by a change in supercell, and a 10 Å vacuum (Table S1) is added in the z-direction to prevent interactions between the periodic images.[23,39,45] This results in the lattice vector for Mo_2CO_2 $3 \times 3 \times 1$ is a=9.20 Å, b=9.20 Å, c=15.00 Å, α=90°, β=90°, and γ=120°. The bottom three layers were frozen during Mo_2CO_2 optimization. All the DFT simulations were performed using the Quantum Espresso-7.1 software package. [46] The calculation of the exchange-correlation energy was performed using the GGA-PBE method, where GGA is a generalized gradient approximation employed with the parameters provided by Perdew, Burke, and Ernzerhof, with spin-polarization. [47,48] A 36 Ry for cut-off energy, 3×3×1 k-point for Brillouin zone, and DFT-D3 for van der Waals interactions were employed during the calculations.[49] The optimization of the structural geometry was allowed to proceed to the force and energy, which attained values of 2.0×10^{-2} Ry/a.u. and 1.0×10^{-5} a.u., respectively. Image visualization was performed using Vesta software.[50] To understand the stability of the single atom, Mo_2CO_2 binding energy calculations are performed using the following formula. [51]

View Article Online
DOI: 10.1039/D6NA00397D

$$E_b = E_{PSA-Mo_2CO_2} - E_{PSA} - E_{Mo_2CO_2} \quad (1)$$

Where E_b, $E_{PSA-Mo_2CO_2}$, E_{PSA}, and $E_{Mo_2CO_2}$ represent the binding energy of a p-block single atom, the total energy of a p-block single atom anchored on Mo_2CO_2, the p-block single atom electronic energy, and the electronic energy of bare Mo_2CO_2, respectively. The Gibbs free energy was calculated for all intermediates present in the electrochemical reduction reaction process using the computational hydrogen electrode (CHE) method. [52]

$$\Delta G = \Delta E_{DFT} + \Delta ZPE - T\Delta S \quad (2)$$

ΔG, ΔE_{DFT}, ΔZPE, T, and ΔS refers to the change in Gibbs free energy, DFT electronic energy for reaction, zero point energy change, temperature, and entropy change, respectively. Entropy and zero-point energy for gaseous molecules and intermediates formed during the reaction are considered, as reported in the literature.[18,53,54] Entropy contributed by gaseous molecules such as CO_2, H_2, and H_2O is considered from the NIST database (Table S2), while the entropy contributed by the solid phase intermediate is neglected. [55,56]

The adsorption energy is calculated by using the following equation.

$$E_{ads} = E_{total} - E_{adsorbate} - E_{catalyst} \quad (3)$$

E_{ads} is the adsorption energy, E_{total} is the total energy of the system (adsorbate + catalyst), $E_{adsorbate}$ is the electronic energy of the adsorbate, $E_{catalyst}$ is the electronic energy of the catalyst.

The cohesive energy of the system is calculated using the following formula.

$$E_{coh} = \frac{E_{catalyst} - (n_{Mo}E_{Mo} + n_C E_C + n_O E_O + n_{PSA}E_{PSA})}{n_1 + n_2 + n_3 + n_4} \quad (4)$$

View Article Online
DOI: 10.1039/D6NA00397D

The n_{Mo}, n_C, n_O, and n_{PSA}, represents the number of molybdenum, carbon, oxygen and p-block single atoms, respectively, present in the catalyst and E_{Mo}, E_C, E_O, and E_{PSA}, $E_{catalyst}$ denotes the energy of molybdenum, carbon, p-block single atom, and the catalyst total energy, respectively. The $n_1 + n_2 + n_3 + n_4$ represents the total number of atoms.

Limiting potential is calculated by the formula given below.

$$U_L = -\Delta G_{max}/e \quad (5)$$

ΔG_{max} is the maximum Gibbs free energy barrier of the potential determining step (PDS), and e represents an electron.[57]

3. Result and discussion

3.1 Structure and stability of PSA@Mo_2CO_2

Mo_2C exhibits a hexagonal structure and is formed by a three-layer Mo-C-Mo, where the upper and lower layers are made of Mo, and the middle layer is carbon. A previous study demonstrated that Mo_2C can be synthesized experimentally and its surface can be functionalized with O, F, or OH.[58]However, oxygen surface functionalization is more stable than other surface functionalizations. [44,59] The calculated Mo–Mo and Mo–C bond lengths were found to be 3.07 Å and 2.07 Å, respectively, which are similar to those reported in previous computational and experimental studies.[58,60] This work initially investigates the PSA stability in various coordination environments on the Mo_2CO_2 two-dimensional nanomaterial support at the atomic level. The 23 PSA were anchored on bare Mo_2CO_2, except for the radioactive one, to avoid environmental problems and considering safety measures. The PSA stability on three different sites (hollow-C (S1), hollow-Mo (S2), and top-O (S3)) is considered on Mo_2CO_2 with different coordination

View Article Online
DOI: 10.1039/D6NA00397D

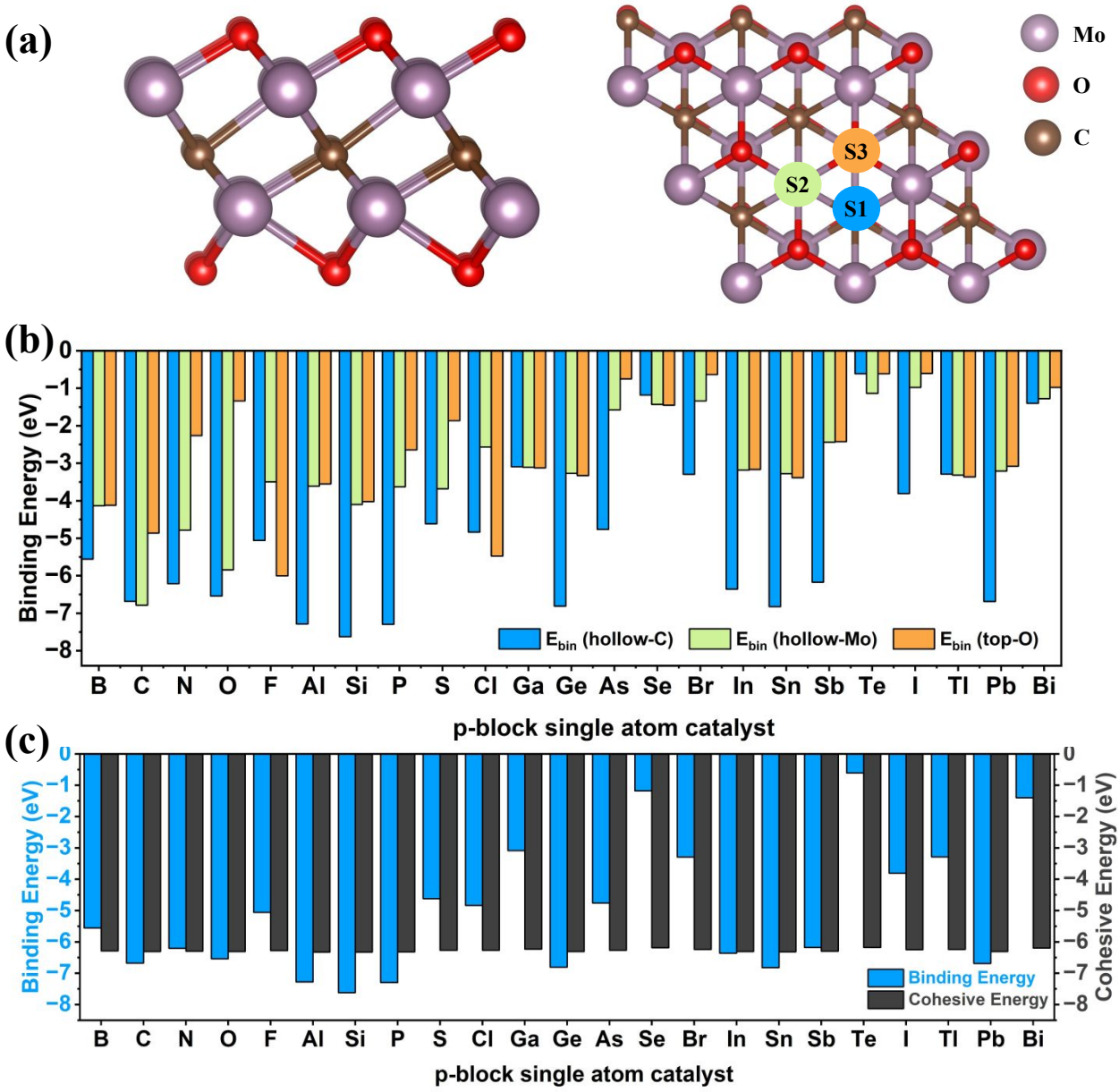

Fig. 1. (a) Side and top views of the Mo_2CO_2 optimized structure, (b) The binding energy of a PSA anchored on Mo_2CO_2 on three different sites: hollow-C (S1), hollow-Mo (S2), and top-O (S3), and (c) Comparison between binding energy versus cohesive energy of PSA@Mo_2CO_2.

View Article Online
DOI: 10.1039/D6NA00397D

environments (Fig. 1(a)). The PSA anchored on the hollow-C site of Mo_2CO_2, coordinating with oxygen and molybdenum atom present on the surface of Mo_2CO_2. For hollow Mo site, PSA is anchored on Mo site only, whereas top-O site PSA is anchored only with oxygen atom. All these sites were considered to find the most preferable site for PSA on Mo_2CO_2. For being a better catalyst, it should be thermodynamically stable. The PSA@Mo_2CO_2 thermodynamic stability is explained by the binding energy, which indicates the strength of the interaction between PSA and Mo_2CO_2. The calculated binding energy reveals that the PSA@Mo_2CO_2 exhibits a negative binding energy, suggesting that it is thermodynamically stable and that the catalyst can be synthesized experimentally. [23,61] All hollow-C (S1), hollow-Mo (S2), and top-O (S3) site optimized structures of PSA@Mo_2CO_2 are shown in Fig. S3-S5. Among all adsorption sites, the binding energy of the majority of PSA on the hollow-C (S1) site is lower than that on the hollow-Mo (S2) and top-O (S3) sites, as shown in Fig. 1(b), indicating that out of all sites, most of the PSA is thermally stable on the hollow-C site (S1). This is due to the weaker repulsion from the surrounding atoms at the hollow-C site [23], which is the main reason to consider it for further studies. Out of 23 PSA, silicon shows the lowest binding energy (−7.63 eV), indicating that silicon is the most stable single atom on the Mo_2CO_2 surface and binds strongly to the oxygen site.[62,63] Chen et al. [64] reported that amorphous SiO_2 with an excess oxygen defect exhibits a Si–O bond length of approximately 1.90 Å, similar to the reported value for Si@Mo_2CO_2. The average bond length of Si anchored on the oxygen surface of Mo_2CO_2 is lower than the previously published study value of 2.79 Å, demonstrating that Si is most stable on the oxygen surface of Mo_2CO_2 due to a shorter bond length compared to the previous study of Si anchored on the Mo of Mo_2CO_2.[39] Silica (β-cristobalite) shows covalent bonding, with a bond length for Si–O of approximately 1.61 Å. [65,66] Whereas the Si@Mo_2CO_2, Si–O bond length (1.90 Å) shows a weak covalent bond as the

View Article Online
DOI: 10.1039/D6NA00397D

bond length elongates. Halogens (F, Cl, Br, and I) are unstable at the carbon top position and shift near molybdenum, as halogens tend to coordinate better with metal to minimize repulsion from the surface termination group.[67] Therefore, they are not considered for further studies. Furthermore, to gain a better understanding of the bonding interaction between PSA and Mo_2CO_2, the calculated average bond length of PSA@Mo_2CO_2 is presented in Table S3 of the supporting information**.** The atomic radius of PSA generally increases going downward the group from B to Tl, C to Pb, N to Bi, and O to Te. However, when the PSA is anchored on Mo_2CO_2, the average bond length between the PSA and Mo_2CO_2 neighbouring atoms shows variation, as the PSA is anchored on either the oxygen or molybdenum site of Mo_2CO_2. In the case of the 14th group element, the average bond length from C to Si decreases from 1.99 Å to 1.90 Å, and Si to Pb increases from 1.90 Å to 2.35 Å, because carbon is anchored with Mo site and Si, Ge, Sn, and Pb are anchored on oxygen surface of Mo_2CO_2, and atomic radius of Mo is greater than O, that leads to increase average bond length. Next, in the case of the 15th group element from As to Bi, the average bond length increases down the group from 1.88 Å to 2.57 Å, except for N (1.95 Å) and P (2.19 Å). As N is anchored on Mo of Mo_2CO_2 and P is anchored on both Mo and O of Mo_2CO_2, which shows a different nature of increase in bond length, due to the increase in atomic radius of Mo than O. At last 16th group element average bond length follows an increasing trend from O (2.00 Å) to Se (2.58 Å) except Te (2.57 Å), Because O, S, and Se are anchored with Mo and Te is anchored with oxygen and Mo, this leads to the difference in average bond length.

Furthermore, the stability and clustering ability of PSA on the Mo_2CO_2 surface are evaluated by comparing the binding and cohesive energies. As shown in Fig. 1(c), the calculated cohesive energy is higher than the binding energy for B, N, F, S, Cl, Ga, As, Se, Br, Sb, Te, I, Tl, and Bi; this reveals that PSA is unstable on Mo_2CO_2 surface. However, in the case of PSA (C, O,

View Article Online
DOI: 10.1039/D6NA00397D

Al, Si, P, Ge, In, Sn, and Pb), the Binding energy of C(− 6.68 eV), O (− 6.54 eV), Al(− 7.28 eV), Si(− 7.62 eV), P(− 7.30 eV), Ge(− 6.81 eV), In(− 6.36 eV), Sn(− 6.82 eV), Pb(− 6.69 eV) is lower than cohesive energy C(− 6.31 eV), O (− 6.31 eV), Al(− 6.33 eV), Si(−6.33 eV), P(− 6.33 eV), Ge(−6.31 eV), In(− 6.31 eV), Sn(− 6.32 eV), Pb(− 6.31eV), which indicates that these single atoms can be stable and uniformly anchored on the Mo_2CO_2 surface.[21] Therefore, only C, O, Al, Si, P, Ge, In, Sn, and Pb have been considered for further study.

3.2 CO_2 activation

The CO_2 molecule has C–O1 and C–O2 bond lengths of 1.17 Å and a bond angle of 180°. In the CRR process, the first step is the adsorption and activation of CO_2. Initially, the CO_2 adsorbs onto the catalyst, with two possible adsorption modes: end-on and side-on site adsorption. [68]

In end-on adsorption mode (Fig.S6, Table S4), O1 of the CO_2 adsorbs through a monodentate on PSA@Mo_2CO_2 (C, O, Al, Si, P, Ge, In, Pb, and Sn) and allowed for the energy minimization. This leads to an increase in the bond length of C–O1 from 1.17 Å to a range of 1.17-1.37 Å. Additionally, the bond angle varies from 180° to a range between 127.21° and 179.92°. These results suggest that CO_2 is being activated on the PSA@Mo_2CO_2 (PSA = Al, Si, Ge, In, Sn, and Pb) catalyst surface. Liu et al. [69] reported that the bond length of C–O1 and C–O2 of adsorbed CO_2 on the Al site of γ-Al_2O_3(100) is found to be 1.18 Å and 1.17 Å, indicating that CO_2 activation is more favorable on Al@Mo_2CO_2 compared to γ-Al_2O_3(100). Additionally, CO_2 on Sn@Mo_2CO_2 shows similar bond length and angle as observed on SnO_2(110) catalyst reported by wang et al.[70] In the case of side-on adsorption (Fig. S7, Table S5), CO_2 tends to adsorb as a bidentate mode through the carbon and the O1 atom on PSA@Mo_2CO_2 (PSA=C, O, Al, Si, P, Ge, In, Sn, and Pb), and allowed for the geometry optimization. The resulting geometries show that the CO_2 molecule has varied structural features, with bond lengths ranging from 1.17 Å to 1.42 Å and bond angles

View Article Online
DOI: 10.1039/D6NA00397D

ranging from 129.32 ° to 179.92 °. Among all, based on CO_2 structural features, it is found that Si effectively activates CO_2, consistent with the results of Mao et al. [71] The adsorption of CO_2 on Si@Mo_2CO_2 shows weak adsorption energy (− 0.03 eV). The energy of CO_2 adsorption comes under the physisorption range. However, after CO_2 adsorption, CO_2 bond length (C − O1=1.42 Å and C − O2=1.19 Å) and angle (129.32°) changed significantly from its linear structure with bond length (C − O1=1.17 Å and C − O2=1.17 Å) and bond angle (180°). The significant change in the structural features of CO_2 is supported by the Bader charge and charge density difference. The Bader charge analysis shows that after adsorption of CO_2 on Si@Mo_2CO_2 (C= + 0.96 e, O1= − 1.10 e, and O2= − 1.02 e) shows charge transfer between CO_2 and Si@Mo_2CO_2 as shown in Table S6 compared to neutral linear CO_2 (C= + 2.06 ,O1= − 1.03 e, and O2= − 1.03 e) molecule. This is also confirmed by the charge density difference of CO_2 adsorbed Si@Mo_2CO_2 (Fig. S8). The charge density difference for CO_2 adsorbed Si@Mo_2CO_2 shows charge depletion on C and O2 and accumulation on O1. The structural change, Bader charge (Table S6), and charge density difference (Fig. S8) indicate that adsorption of CO_2 on Si@Mo_2CO_2 is chemisorption. This observation aligns well with the previous study, which showed that weakly adsorbed bent CO_2 on reconstructed Cu_2O(111) undergoes chemisorption due to significant charge transfer.[72]

For the C, O, P, and Ge-based PSA@Mo_2CO_2, there are no significant structural features of CO_2 observed when it is in the side-on and end-on configurations. Therefore, these PSA@Mo_2CO_2 were not considered for further analysis. Whereas on Al, Si, In, Sn, and Pb, after optimization, side-on and end-on show the bond length (C–O) and angle (O–C–O) variation. Based on the bond distance between PSA and O1 of the CO_2 and Bader charge analysis (Table S6), Al@Mo_2CO_2 and Si@Mo_2CO_2 show chemisorption among all PSA, as shown in Table S5-S6.

View Article Online
DOI: 10.1039/D6NA00397D

3.3 Electronic structure analysis for Mo_2CO_2 and PSA@Mo_2CO_2

The projected density of states (PDOS) analysis was performed to elucidate the electronic properties of Mo_2CO_2 and PSA@Mo_2CO_2 and to explain the orbital interaction between PSA and the oxygen surface of Mo_2CO_2.[14] For Mo_2CO_2, as shown in Fig. 2(a), below the Fermi level, the Mo d-orbital electronic state intensity was lower, and the O valence p-orbital electronic state intensity was higher. In contrast, Mo contributes more to the conduction band above the Fermi level. At the same time, oxygen exhibits a low-intensity electronic state in the conduction band, indicating electron transfer from Mo to O.

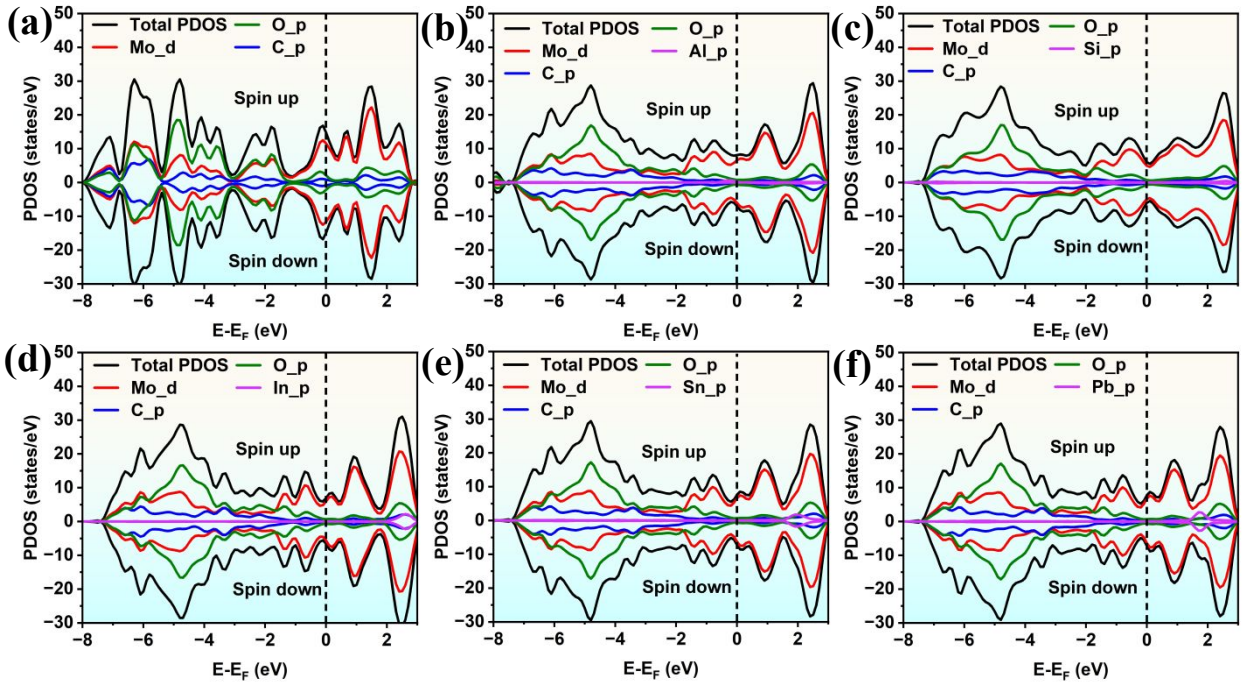

Fig. 2. PDOS for (a) Mo_2CO_2 and (b-f) PSA@Mo_2CO_2 (PSA = Al, Si, In, Sn, and Pb), with the Fermi level indicated by a black dashed line. Below the Fermi level is the valence band, and above the Fermi level is the conduction band on the x-axis.

View Article Online
DOI: 10.1039/D6NA00397D

Additionally, the Mo-d and O-p valence peaks overlap effectively, indicating a strong interaction between the Mo-d and O-p valence orbitals. Therefore, Mo_2CO_2 is stable with an O-terminated surface.[17] The PDOS plot in Fig. 2(a) indicates that Mo_2CO_2 exhibits a metallic-like nature, characterized by a zero-band gap, as the molybdenum and oxygen valence band peaks align with the Fermi level. [39] However, the introduction of the p-block element shifts the valence band near the Fermi level. In Fig. 2(b), the Al valence p-orbital peak passes through the Fermi value ($E-E_F = -0.30$ eV), resulting in $Al@Mo_2CO_2$ exhibiting metallic-like behavior, and the Al valence p-orbital overlaps with the O valence p-orbital, showing p-p orbital hybridization, indicating that Al strongly binds and is stable on the oxygen surface of the Mo_2CO_2 support. The Al p-orbital electronic state on the conduction band side shows transfer of an electron from Al to Mo_2CO_2, which is confirmed by the Bader charge of Al (+1.79 e) and the charge density difference of $Al@Mo_2CO_2$, Fig. 3(e). The $Al@Mo_2CO_2$ with the most positive Bader charge exhibited the most stable CO_2 adsorption with an adsorption energy of -0.97 eV. Fig. 2(c), The Si-p and O-p valence orbital overlap near the Fermi level shows strong p-p hybridization and bonding between Si and O of Mo_2CO_2. The Si-p orbital electronic state in the conduction band ($E-E_F=2.60$ eV) side shows transfer of an electron from Si to Mo_2CO_2, which is confirmed by the Bader charge of Si (+1.65 e) and charge density difference as shown in Fig. 3(f). $Si@Mo_2CO_2$ exhibits a metallic-like character due to a non-zero electronic state at the Fermi level. Furthermore, the charge density difference shows charge transfer between Si and CO_2, as shown in the supporting information (Fig. S8). The carbon in CO_2 is electrophilic in nature, gets an electron from Si, and donates an electron from nucleophilic oxygen to Si and adsorbs by side-on mode with weak adsorption ($E_{ads} = -0.03$ eV). In shows a low-intensity p-orbital near the Fermi level compared to the Si-p orbital (Fig. 2(d)) and overlaps with the O-p orbital, indicating lower stability of In on the oxygen of Mo_2CO_2

View Article Online
DOI: 10.1039/D6NA00397D

compared to Si. The In@Mo_2CO_2 exhibits metallic-like behavior because the valence band crosses the Fermi level. Figure 2(e-f) shows that Sn-p and Pb-p contribute near the Fermi level. The Pb-p orbital electronic state on the conduction-band side shows an electronic state near the Fermi level, compared to the Sn-p orbital. This indicates less electron transfer from Pb than from Sn to the Mo_2CO_2 surface. This is confirmed by the Bader charge analysis of Sn (+1.40 e) and Pb (+1.37 e). The Sn p-orbital shows moderate electron transfer to CO_2 with moderate adsorption energy (− 0.15 eV) compared to Pb (− 0.23 eV). The valence band p-orbital peak intensity for PSA(Al, Si, In, Sn, and Pb) near the Fermi level side is in the order of Si>Al>Sn>Pb>In. This leads to greater charge transfer from Si and Al after CO_2 adsorption, as confirmed by the charge-density difference shown in the supporting information (Fig. S8). Figure S9 (a-e) represents the PDOS for PSA@Mo_2CO_2. The electronic state present on the valence band side ($E-E_F$=0 to − 8 eV) below the Fermi level for the Si-p orbital is more populated compared to the Al, In, Sn, and Pb p-orbital electronic states. The In p-orbital electronic state intensity is very low, whereas Al and Pb have p-orbital electronic state intensity more than In. The Sn shows optimal electronic state intensity on the valence-band side. This facilitates *OCHO intermediate adsorption as evident from the adsorption energy (− 2.78 eV), which is more favorable for the electrochemical CRR. Where Si@Mo_2CO_2 (− 4.35 eV) has the lowest adsorption energy and adsorbs strongly *OCHO. The Pb@Mo_2CO_2 (− 2.33 eV) has a higher adsorption energy for *OCHO compared to Sn@Mo_2CO_2 (− 2.78 eV). The Al@Mo_2CO_2 (− 1.81 eV) shows poorer adsorption of the intermediate than PSA@Mo_2CO_2 (PSA=Si, Sn, and Pb). The addition of PSA broadens the band, increases charge transfer, and facilitates intermediate adsorption for electrocatalytic CRR.

View Article Online
DOI: 10.1039/D6NA00397D

3.4 Bader charge and charge density difference analysis for PSA@Mo_2CO_2

The Bader charge analysis was performed to deepen the understanding of charge transfer in Mo_2CO_2 and PSA@Mo_2CO_2. The charge is analyzed before and after PSA anchoring on Mo_2CO_2. Figure S10(a) represents a uniformly distributed charge on bare Mo_2CO_2, where O and Mo have -1.01 e and $+1.71$ e charge. Figure S10(b-e) shows that after anchoring PSA (Al, Si, In, Sn, and Pb) on Mo_2CO_2, charge transfer from PSA to neighboring Mo and O of Mo_2CO_2. Figure S10(b) displays that after Al is anchored on Mo_2CO_2, Bader charge on Mo ($+1.56$ e, $+1.49$ e, $+1.57$ e) and O (-1.33 e, -1.32 e, -1.25 e) increases. In Si@Mo_2CO_2 Fig. S10(c) charge is transferred from Si to Mo ($+1.60$ e, $+1.60$ e, $+1.56$ e) and O (-1.34, -1.35 e, -1.09 e). In case of In@Mo_2CO_2 (Fig. S10 (d)), charge transfer from In to Mo ($+1.64$ e, $+1.59$ e, $+1.65$ e) and O (-1.05 e, -1.13 e, -1.13 e). In Sn@Mo_2CO_2 (Fig. S10(e)), charge transfer from Sn to Mo ($+1.58$ e, $+1.53$ e, $+1.58$ e) and O (-1.08 e, -1.19 e, -1.19 e). For Pb@Mo_2CO_2 (Fig. S10. (f)), charge transfer from Pb to Mo ($+1.59$ e, $+1.53$ e, $+1.58$ e) and O (-1.09 e, -1.16 e, -1.16 e). Out of all PSA@Mo_2CO_2 (PSA = Al, Si, In, Sn, and Pb), Sn($+1.40$ e) has an optimal charge. Further, the Bader charge is calculated after CO_2 adsorption on PSA@Mo_2CO_2. The Bader charges on Al, Si, In, Sn, and Pb were +2.43 e, +3.00 e, +0.86 e, +1.41 e, and +1.40 e, respectively. Bader charge analysis shows that the charge transfer is negligible for In. Therefore, it is considered less active for CRR and is excluded from further analysis. In the case of Al@Mo_2CO_2 and Si@Mo_2CO_2, Bader charge significantly changes after CO_2 adsorption, which shows changes in bond angle(length) are 175.39°(C – O1=1.20 Å and C – O2=1.15 Å) and 129.32° (C – O1=1.42 Å and 1.19 Å), respectively. Whereas, in the case of Sn@Mo_2CO_2 and Pb@Mo_2CO_2, very little charge transfer occurs when CO_2 is adsorbed, which shows negligible variation in the bond angle(length) are

View Article Online
DOI: 10.1039/D6NA00397D

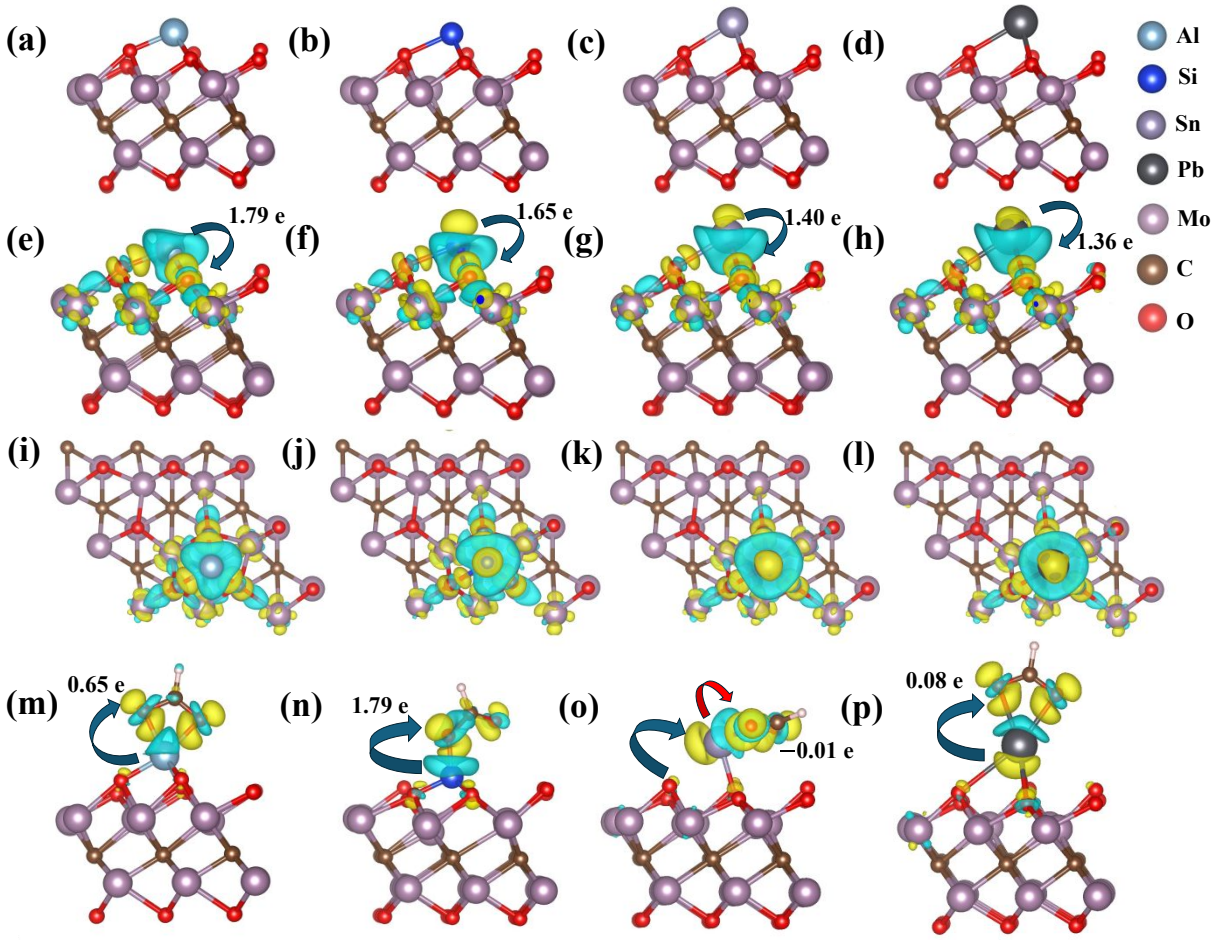

Fig. 3. Optimized geometry of (a) Al@Mo_2CO_2, (b) Si@Mo_2CO_2, (c) Sn@Mo_2CO_2, and (d) Pb@Mo_2CO_2. The Charge density difference side view of (e) Al@Mo_2CO_2, (f) Si@Mo_2CO_2, (g) Sn@Mo_2CO_2 and (h) Pb@Mo_2CO_2, and the top view of (i) Al@Mo_2CO_2, (j) Si@Mo_2CO_2, (k) Sn@Mo_2CO_2, and (l) Pb@Mo_2CO_2. The charge density difference for the *OCHO intermediate adsorbed on (m) Al@Mo_2CO_2, (n) Si@Mo_2CO_2, (o) Sn@Mo_2CO_2, and (p) Pb@Mo_2CO_2; yellow and cyan indicate charge accumulation and depletion, respectively, with an isosurface value of 0.005 e/Å^3. The blue arrow shows transfer of charge from PSA to *OCHO intermediate (except Sn), In case of Sn, blue arrow shows charge transfer from Mo_2CO_2 to Sn and the red arrow displays Sn to *OCHO charge transfer.

View Article Online
DOI: 10.1039/D6NA00397D

179.45°(C ─ O1=1.18 Å and C ─ O2=1.17 Å) and 179.82° (C ─ O1=1.18 Å and C ─ O2=1.17 Å) respectively (Table S5).

As seen in Fig. 3(a-d), the optimized structure of PSA@Mo_2CO_2 (where PSA represents Al, Si, Sn, and Pb) is considered for further study. Fig. 3(e-h) displays the charge density difference (CDD) side view, and Fig. 3(i-l) shows the top view of PSA@Mo_2CO_2. The CDD analysis is utilized to understand the distribution of charge density on PSA@Mo_2CO_2. The positive charge region exhibits a depletion of charge density, indicated by the cyan-colored region, and the negative charge region shows charge accumulation; electrons are concentrated in this region, represented by the yellow color. The Al@Mo_2CO_2, Si@Mo_2CO_2, Sn@Mo_2CO_2, and Pb@Mo_2CO_2 show charge transfer from Al, Si, Sn, and Pb to Mo_2CO_2.[23,32,73] Most of the electron gained by oxygen, which is shown by yellow colour, and cyan color present on Mo displays charge transfer from Mo to O, out of Al, Si, Sn, and Pb, more charge accumulated on Si followed by Pb, Sn and Al, which indicate Si can donate and accept electron, Sn and Pb have lower number of electrons. The Bader charges on Al@Mo_2CO_2 (+1.79 e), Si@Mo_2CO_2 (+1.65 e), Sn@Mo_2CO_2 (+1.40 e), and Pb@Mo_2CO_2 (+1.37 e) align with a CDD study, which shows that Al shows charge depletion due to maximum electron transfer. Si shows charge accumulation and charge depletion due to partial charge transfer from Si to Mo_2CO_2. In contrast, Sn shows greater charge depletion and less charge accumulation than Pb, as shown in Fig. 3(k-l) (top view). This is because most of the electron transfer occurs from Sn and Pb to Mo_2CO_2. This is due to the metallic properties of Al, Sn, and Pb, as metals can donate their electrons more readily than Si, which is a metalloid.

Figure 3(m-p) displays the charge transfer between *OCHO intermediate, and PSA, and Mo_2CO_2 surface. Figure 3(m-n) shows higher charge transfer from Al and Si to *OCHO, whereas Pb shows lower charge transfer (Fig. 3(p)). The cyan color present on Al, Si, Sn, and Pb indicates charge

View Article Online
DOI: 10.1039/D6NA00397D

depletion, with the charge transferred from PSA to *OCHO. The yellow color present on the *OCHO intermediate shows charge gain. Among all PSAs, Sn shows distinct charge transfer, as shown in Fig. 3(o). Charge is transferred from the Mo_2CO_2 surface to Sn and, further, Sn to *OCHO intermediate as shown in Fig. S11, due to which Sn shows distinct Bader charge transfer after adsorption of *OCHO on Sn@Mo_2CO_2. The overall Bader charge on Sn is -0.01 e after *OCHO intermediate adsorption on Sn@Mo_2CO_2.

3.5 Reaction mechanism for CRR and HER

The electrochemical CRR is challenging and complicated; therefore, an effective catalyst is required. The reduction of CO_2 to CO and HCOOH on a catalyst surface is a two-step, two-electron pathway that proceeds via a twice-proton-coupled electron-transfer reaction, as shown in Fig. 4, which is widely proposed as the path and accepted as the most likely one. The first step in CO_2 reduction involves the acceptance of a proton and an electron, leading to two possible competitive intermediates, *OCHO and *COOH. This indicates that there are two pathways: either the carbon or the oxygen site of CO_2 can receive a proton and an electron. Further, proton and electron transfer occur, and the *OCHO and *COOH intermediates are converted into *HCOOH and *CO, respectively. In the last step, *HCOOH and *CO desorb from the catalyst surface, forming HCOOH and CO products. [74] In contrast, the selectivity toward CH_4 and CH_3OH depends on the adsorption of the *CO intermediate. If the adsorption of *CO is weaker, it will terminate at the CO product. As shown in Fig. 5 (a-f), Gibbs free energy for PSA@Mo_2CO_2 *CO intermediate is weaker. Therefore, CO_2 does not reduce to CH_3OH and CH_4.[75] Furthermore, the p-block metals In, Sn, and Pb are known for electrochemically reducing CO_2 to HCOOH, with Faradaic efficiencies exceeding 90%. CH_3OH and CH_4 follow six- and eight-electron pathways,

View Article Online
DOI: 10.1039/D6NA00397D

respectively, whereas HCOOH follows a two-electron pathway.[76] Therefore, CO_2 reduction is not further considered for CH_4 and CH_3OH.

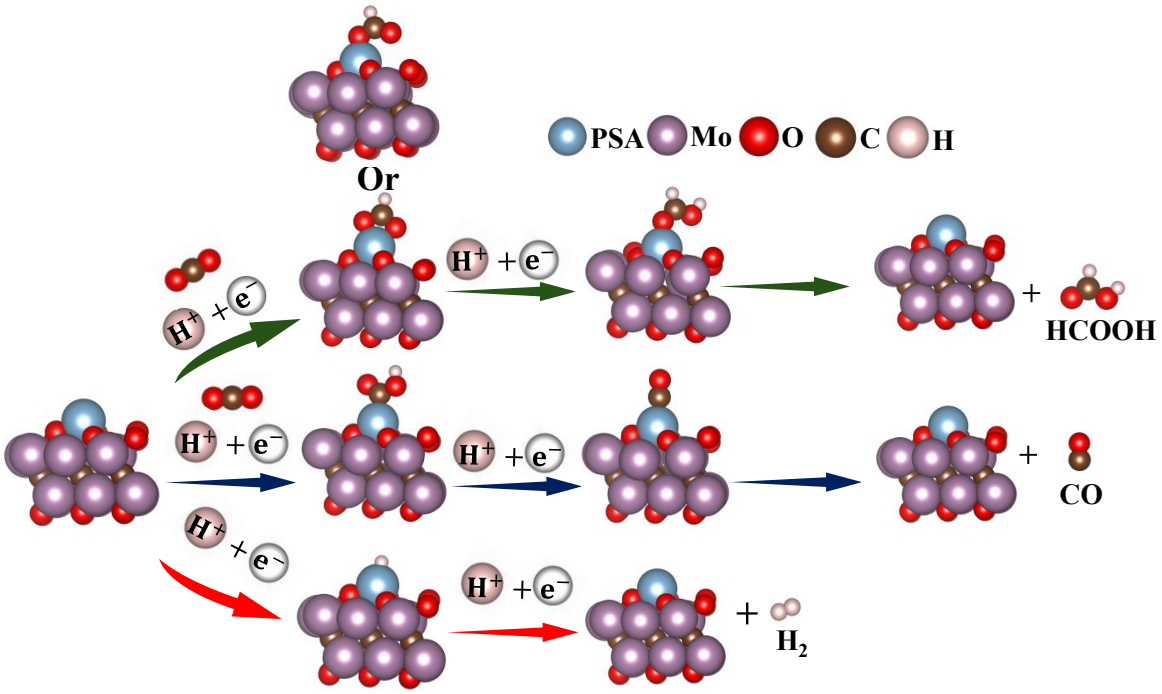

Fig. 4. Schematic illustration of the reaction mechanism for electrochemical CRR to CO and HCOOH products and competitive HER on the catalyst surface. For the HCOOH product, there are two possible binding sites for the intermediate(*OCHO), one oxygen site or two oxygen sites.

The energy-minimized structures of all intermediates involved in the CRR on the surfaces of the Mo_2CO_2 and PSA@Mo_2CO_2 (Al, Si, Sn, and Pb) catalysts are displayed in Fig. S12**.** The Gibbs free energy diagram for CRR on Mo_2CO_2 and PSA@Mo_2CO_2 surface is shown in Fig. 5. For the bare Mo_2CO_2 surface (Fig. 5(a)), the Gibbs free energy for the first step, CO_2 into *OCHO and *COOH intermediates, is 1.60 eV and 1.05 eV, respectively. The calculated values suggest that the *OCHO and *COOH intermediates are present as PDS with the maximum Gibbs free energy change (Table S8 and S9). [61] Among the intermediates, the *COOH intermediate formation is

View Article Online
DOI: 10.1039/D6NA00397D

more favorable with a lower Gibbs free energy change in the first step compared to *OCHO. Therefore, the subsequent formation of CO is more favorable than that of HCOOH. On Al@Mo_2CO_2 (Fig. 5(b)), the calculated Gibbs free energy change value suggests that *COOH (3.53 eV) and *OCHO (1.56 eV) are the PDS for the CO and HCOOH (Table S8 and S9), respectively. This result shows that *OCHO intermediate formation is more favorable compared to *COOH due to the lower Gibbs free energy change. Therefore, HCOOH product formation is preferred on Al@Mo_2CO_2, consistent with the earlier report.[77] Furthermore, the Gibbs free energy plot for CO_2 reduction on the Si@Mo_2CO_2 surface (Fig. 5(c)) reveals that the conversion of *COOH to *CO and *OCHO to *HCOOH is found to be PDS, with a maximum Gibbs free energy change of 1.69 eV and 2.34 eV, respectively (Table S8 and S9). This indicates that Si@Mo_2CO_2 promotes the formation of CO rather than HCOOH. The Sn@Mo_2CO_2 (Fig. 5(d)) catalyst surface shows that the *+ CO_2 to *COOH and *OCHO conversion steps are found to be the PDS with Gibbs free energy change of 1.95 eV and 0.58 eV, respectively (Table S8 and S9). This indicates that the HCOOH product is preferred over the CO product. In the case of Pb@Mo_2CO_2 surface (Fig. 5(e)), the PDS for the *+CO_2 to *OCHO and *COOH shows a Gibbs free energy change of 1.03 eV and 2.32 eV, respectively (Table S8 and S9). This indicates that it favors the formation of HCOOH, as its Gibbs free energy change is lower than that for the formation of CO. Out of all the catalysts, the Sn@Mo_2CO_2 surface exhibited the lowest Gibbs free energy change for HCOOH formation from CO_2.

The reason for the Gibbs free energy difference between *COOH and *OCHO intermediate on PSA@Mo_2CO_2 (PSA=Al, Si, Sn, and Pb) is elucidated using Bader charge analysis. This deepens the understanding of CO and HCOOH reaction pathway and PSA@Mo_2CO_2 catalytic activity. The Gibbs free energy for *OCHO intermediate on PSA@Mo_2CO_2, (PSA=Al(1.56 eV),

View Article Online
DOI: 10.1039/D6NA00397D

Si(− 0.99 eV), Sn(0.58 eV), and Pb(1.03 eV)) is found to be lower as compared to that of the Gibbs free energy for *COOH intermediate on PSA@Mo_2CO_2, (PSA=Al(3.53 eV), Si(− 0.05 eV), Sn(1.95 eV), and Pb(2.32 eV)). The Bader charges present on PSA of PSA@Mo_2CO_2 (PSA=Al(+ 1.79 e), Si(+ 1.65 e), Sn(+ 1.40 e) and Pb(+ 1.37 e)) before intermediate adsorption are shown in Table S7. After *COOH and *OCHO adsorption on PSA@Mo_2CO_2, the Bader charge present on PSA of PSA@Mo_2CO_2 increases (except Sn), as shown in Table S7. Whereas Sn has a Bader charge decreased for *COOH and *OCHO. Interestingly, *OCHO charge transfer is higher than that of *COOH. The *OCHO intermediate adsorption is preferred on the positive charge region, as the oxygen of *OCHO behaves as a nucleophile.[35] This charge transfer makes *OCHO interact more strongly with PSA@Mo_2CO_2, thereby lowering the Gibbs free energy.

Whereas in the case of Sn@Mo_2CO_2, Sn receives a charge from the Mo_2CO_2 support and transfers an electron to the intermediate *OCHO, as shown in the supporting information (Fig. S11(a-e)). This demonstrates that Sn behaves as a good mediator in modulating the charge transfer between intermediate and Mo_2CO_2.[34] Furthermore, Mo_2CO_2 potential role in charge transfer is explored in detail through Bader charge analysis and charge density difference (Fig. S11 (a-e)). First, the Mo_2CO_2 surface Bader charge is calculated, which shows − 1.01 e present on every oxygen atom and + 1.71 e present on every molybdenum atom. After that, a single-atom Sn is anchored on Mo_2CO_2 with three coordinated oxygen atoms. The charge present on neighboring Mo and O atoms underwent a significant change. The Bader charge analysis shows a reduction in the positive charge of Mo (+ 1.58 e, + 1.58 e, + 1.53 e) and an increase in the negative charge of O (− 1.19 e, − 1.19 e − 1.08 e) that indicates charge transfer from Sn (+ 1.40 e) to Mo_2CO_2. This is confirmed by charge density difference: Sn@Mo_2CO_2 shows charge depletion on Sn (Fig. S11(d)), indicated by the cyan color, and the yellow color on the oxygen surface indicates charge gain.

View Article Online
DOI: 10.1039/D6NA00397D

At last, the *OCHO intermediate adsorbed on $Sn@Mo_2CO_2$ configuration is shown in Fig. S11(c). After adsorption of *OCHO on the $Sn@Mo_2CO_2$, Sn coordination environment changed from three to one on Mo_2CO_2. The positive charge present on neighboring Mo (+ 1.59 e, + 1.56 e, + 1.71 e) increases and a negative charge is present on O (− 1.00 e, − 1.05 e, − 1.08 e) decreases further, indicating that the overall charge decreases on the surface of Mo_2CO_2. This shows that the charge transfer occurs from Mo_2CO_2 to Sn. The charge present on Sn (+ 1.39 e) shows a slight decrease in positive charge and tries to maintain its own charge by accepting electrons from the support Mo_2CO_2 and transferring to the *OCHO intermediate. This is confirmed by charge density difference (Fig. S11). After intermediate *OCHO adsorption on $Sn@Mo_2CO_2$ (Fig. S11(e)), the charge on the oxygen surface decreases compared to $Sn@Mo_2CO_2$ before intermediate adsorption, shown in yellow color. While the charge on Sn increases, shown by the yellow color, indicating charge gain by Sn and Sn transferring charge to the *OCHO intermediate. This distinct behavior of Sn as a mediator between *OCHO and Mo_2CO_2 facilitates the formation of HCOOH with a lower Gibbs free energy change compared to other systems, such as $Al@Mo_2CO_2$, $Si@Mo_2CO_2$, and $Pb@Mo_2CO_2$.

During CRR, HER also occurs in parallel and competes with the CRR process. Fig. 5(f) shows the calculated HER Gibbs free energy profile for the Mo_2CO_2 and $PSA@Mo_2CO_2$ (PSA=Al, Si, Sn, and Pb) catalyst surfaces. According to the Sabatier principle, the interactions between the catalyst and the intermediate should be within an optimal range, neither too low nor too high[78], to improve catalytic activity. The Gibbs free energy change for H*, *OCHO, and *COOH (ΔG_{H*}, ΔG_{*OCHO}, and ΔG_{*COOH}) intermediates are shown in Fig. S13 to provide deeper insights into the CRR versus the HER. For an efficient electrochemical CO_2 reduction reaction, an electrocatalyst

View Article Online
DOI: 10.1039/D6NA00397D

should suppress the hydrogen evolution reaction and accelerate the formation of intermediates towards HCOOH and CO. Therefore, the Gibbs free energy for H*, *OCHO, and *COOH

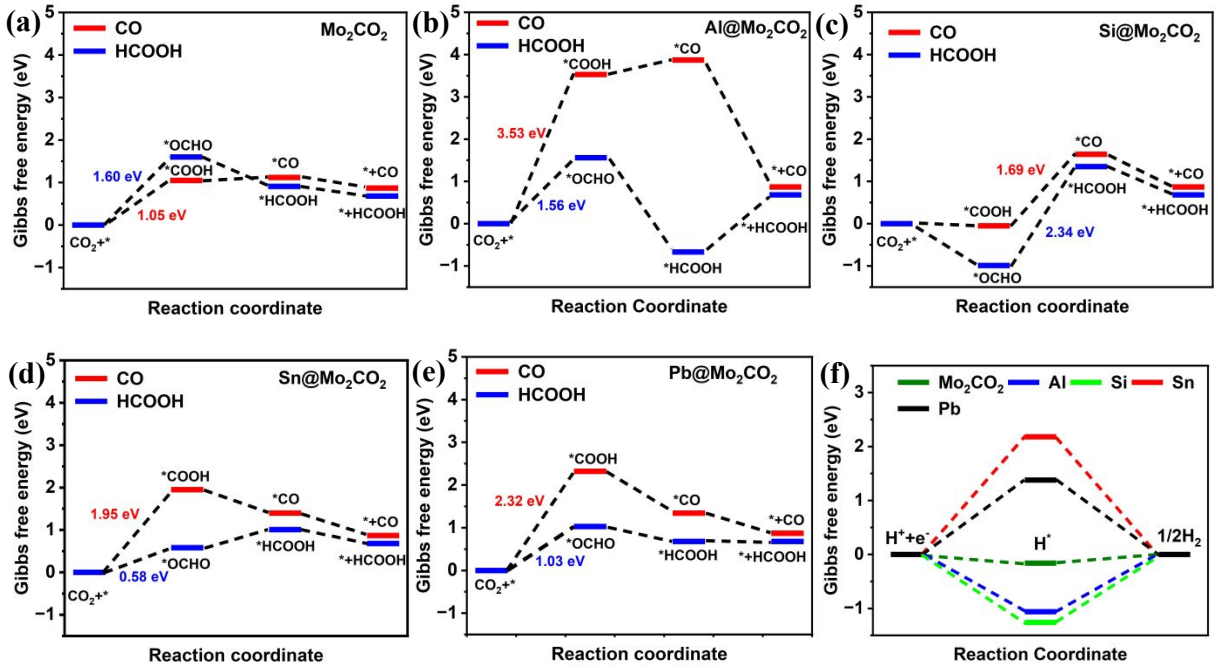

Fig. 5. Gibbs free energy diagram for CO_2+2H$^+$+2e$^-$ to CO and HCOOH product for (a) Mo_2CO_2 and (b-e) PSA@Mo_2CO_2(PSA=Al, Si, Sn, and Pb) and (f) HER Gibbs free energy for Mo_2CO_2 and PSA@Mo_2CO_2 (PSA=Al, Si, Sn, and Pb), where * represents the catalyst surface in all Gibbs free energy diagrams.

intermediates are computed and compared for Mo_2CO_2, Al@Mo_2CO_2, Si@Mo_2CO_2, Sn@MO_2CO_2 and Pb@Mo_2CO_2. The Mo_2CO_2 (-0.16 eV), Al@Mo_2CO_2 (-1.06 eV), and Si@Mo_2CO_2 (-1.26 eV) have lower ΔG for H* compared to *COOH (Mo_2CO_2 (1.05 eV), Al@Mo_2CO_2 (3.53 eV), and Si@Mo_2CO_2 (-0.05 eV)) and *OCHO(Mo_2CO_2 (1.60 eV), Al@Mo_2CO_2 (1.56 eV), and Si@Mo_2CO_2(-0.99 eV)). Therefore, H* adsorption will inhibit the *COOH and *OCHO formation. Whereas in the case of Sn@Mo_2CO_2 (0.58 eV) and Pb@Mo_2CO_2 (1.03 eV), for *OCHO, Gibbs free energy is lower compared to *COOH (Sn@Mo_2CO_2 (1.95 eV)

View Article Online
DOI: 10.1039/D6NA00397D

and Pb@Mo_2CO_2 (2.32 eV)) and H* (Sn@Mo_2CO_2 (2.18 eV) and Pb@Mo_2CO_2 (1.38 eV)). This shows Sn@Mo_2CO_2 and Pb@Mo_2CO_2 facilitate *OCHO formation. The Sn@Mo_2CO_2 has a lower ΔG for *OCHO than Pb@Mo_2CO_2, showing that Sn@Mo_2CO_2 facilitates the conversion of CO_2 to HCOOH.

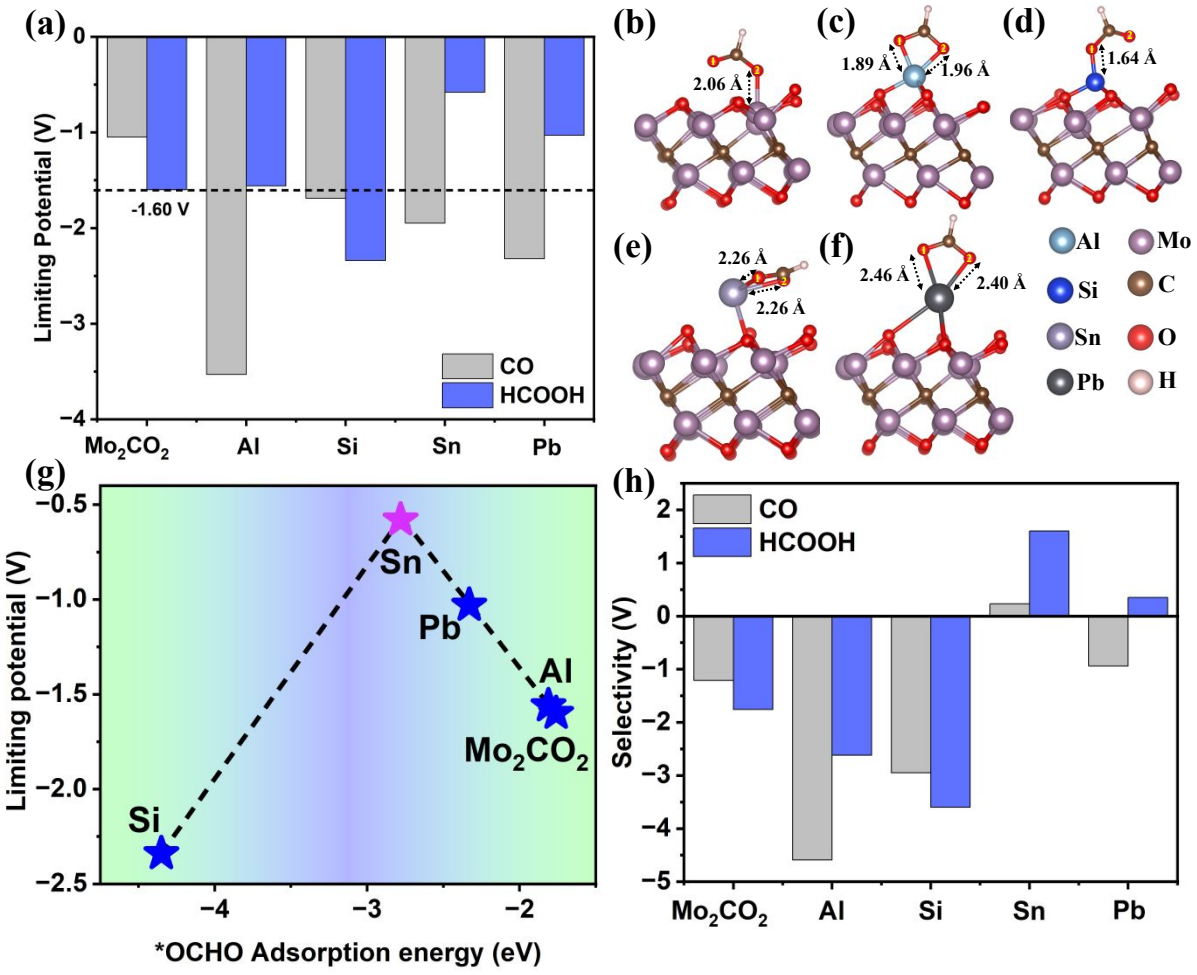

Fig. 6. (a) Limiting potential for CRR (U_L^{CRR}) for HCOOH and CO product on Mo_2CO_2 and PSA @Mo_2CO_2. (b-f) Represents the bond length between the oxygen of the intermediate (*OCHO) and the catalyst (Mo_2CO_2 and PSA@Mo_2CO_2 (g) Volcano plot for PSA@Mo_2CO_2 and Mo_2CO_2 using adsorption energy of *OCHO (E_{ads}) and U_L. (h) Selectivity of CRR toward

View Article Online
DOI: 10.1039/D6NA00397D

CO and HCOOH products. The PSA@Mo_2CO_2 (PSA=Al, Si, Sn, and Pb) is represented as PSA(Al, Si, Sn, and Pb).

The U_L was considered to analyze the electrocatalyst (PSA@Mo_2CO_2) activity. [79] U_L can be defined as the negative maximum difference between the Gibbs free energy of the reaction step ($-\Delta G_{max}$) divided by e (electron). It is used as an electrocatalyst, demonstrating superior performance among all PSA@Mo_2CO_2 electrocatalysts, as shown in Fig. 6 (a). The catalysts exhibit a lower negative value of U_L, which is considered beneficial because low energy is required to overcome the PDS.[57] For Al@Mo_2CO_2, Sn@Mo_2CO_2, and Pb@Mo_2CO_2, the formic acid product pathway is more favorable due to their low negative U_L value −1.56, −0.58, and −1.03 V, respectively, compared to CO product formation as shown in Fig. 6(a), Table S10 and S11. However, for Mo_2CO_2 and Si@Mo_2CO_2, the CO formation pathway is more favorable due to the lower U_L value of −1.05 and −1.69 V, respectively, compared to HCOOH.

3.6 Structure-activity relationship

A suitable structure-activity descriptor is developed to predict the catalytic activity. Here, bond length is considered as a descriptor, and an optimal bond length is required between PSA and *OCHO intermediate to form HCOOH effectively. Fig. 6(b-f) shows how the key intermediate *OCHO adsorbs on Mo_2CO_2 and PSA@Mo_2CO_2. On Mo_2CO_2 and Si@Mo_2CO_2, the *OCHO intermediate strongly adsorbs through a monodentate oxygen site with shorter bond length of 2.06 Å and 1.64 Å, respectively. In the bidentate adsorption mode of *OCHO on Al@Mo_2CO_2, Sn@Mo_2CO_2, and Pb@Mo_2CO_2, the average bond lengths between the O atom and the PSA (Al, Sn, and Pb) are 1.93 Å (Al), 2.26 Å (Sn), and 2.46 Å (Pb). This bidentate adsorption mode resulted in an elongated bond length, causing the weaker adsorption. The bond length for *OCHO adsorbed on Sn@Mo_2CO_2 is shorter than that on Pb@Mo_2CO_2 and longer than that of Al@Mo_2CO_2,

View Article Online
DOI: 10.1039/D6NA00397D

Si@Mo_2CO_2, and Mo_2CO_2. To determine the optimal distance for HCOOH formation, a volcano plot has been constructed. The volcano plot displays a structure activity relationship between the limiting potential and bond length (Fig. S14). As seen in Figure S14, Sn@Mo_2CO_2 is positioned on top of the volcano with the lowest limiting potential and moderate bond length as compared to that of the other catalysts, suggesting that Sn@Mo_2CO_2 favors the formation of HCOOH.

In addition to that, a structure-activity relationship develops between the limiting potential and the adsorption energy of the *OCHO intermediate. Here, adsorption energy is considered as a descriptor, and an optimal adsorption energy is required for HCOOH formation. Feaster et al.[74] plotted a volcano curve using partial current density and binding energy for the elements Ni, Cu, Zn, Sn, Ag, Pt, and Au. Among all, the Sn shows better activity towards CO_2 to HCOOH, as Sn is at the top of the volcano, indicating that the binding is not too high or low for the intermediate *OCHO intermediate. For Al@Mo_2CO_2, Pb@Mo_2CO_2, and Mo_2CO_2 in Fig. 6(g), it is shown that *OCHO intermediate adsorption is weaker, as it may not favor the formation of HCOOH effectively due to the weaker interaction with the catalyst. Whereas Si@Mo_2CO_2 demonstrates strong adsorption of *OCHO intermediate, making it difficult to reduce further to HCOOH. Among Al@Mo_2CO_2, Si@Mo_2CO_2, Sn@Mo_2CO_2, Pb@Mo_2CO_2, and Mo_2CO_2, Sn@Mo_2CO_2 demonstrates the optimal adsorption energy for the *OCHO intermediate, which indicates Sn@Mo_2CO_2 favors the CO_2 reduction into HCOOH. The tilted *OCHO intermediate on Sn@Mo_2CO_2 leads to optimal adsorption of *OCHO intermediate on Sn@Mo_2CO_2 with the lowest limiting potential, and shows on top of the volcano plot as shown in Fig. 6(g).

3.7 Selectivity for CRR to CO/HCOOH

In general, competitive HER hinders CRR at the catalyst surface. If H* adsorbs on the catalyst, then CRR will be inhibited. For effective CRR on catalysts, HER must be avoided at the catalyst

View Article Online
DOI: 10.1039/D6NA00397D

surface. The H* adsorption energy is compared with the adsorption energy of *CO_2 on Mo_2CO_2, Al@Mo_2CO_2, Si@Mo_2CO_2, Sn@Mo_2CO_2, and Pb@Mo_2CO_2 surfaces. It reveals that H* adsorption energy on Mo_2CO_2 (− 0.42 eV), Al@Mo_2CO_2 (− 1.32 eV), and Si@Mo_2CO_2 (− 1.52 eV) is lower compared to the *CO_2 adsorption energy on Mo_2CO_2 (− 0.41 eV), Al@Mo_2CO_2 (− 0.97 eV), and Si@Mo_2CO_2 (− 0.03 eV). From the above results, Mo_2CO_2, Al@Mo_2CO_2, and Si@Mo_2CO_2 will not favor the CRR. However, the H* adsorption energy for Sn@Mo_2CO_2 (1.92 eV) and Pb@Mo_2CO_2 (1.12 eV) is higher compared to the CO_2 adsorption energy for Sn@Mo_2CO_2 (− 0.15 eV) and Pb@Mo_2CO_2 (− 0.23 eV). Hence, Sn@Mo_2CO_2 and Pb@Mo_2CO_2 favor the CRR.[53]

The selectivity between CRR and HER was evaluated to determine the best catalyst among Mo_2CO_2 and PSA@Mo_2CO_2(PSA =Al, Si, Sn, and Pb).[79] The difference between the U_L of CRR and HER defines the selectivity ($U_L^{CRR}-U_L^{HER}$) on the PSA catalyst. A more positive U_L difference ($U_L^{CRR}-U_L^{HER}$) of the value shows that the higher valued one yields the more pronounced selectivity towards CRR.[57] Fig. 6(h) shows the selectivity towards HCOOH on the catalyst surface found in the order of Sn@Mo_2CO_2 > Pb@Mo_2CO_2 > Mo_2CO_2 > Al@Mo_2CO_2 > Si@Mo_2CO_2. This result suggests that Sn@Mo_2CO_2 exhibits the best activity and selectivity for the conversion of CRR to HCOOH.

3.8 Orbital interaction analysis

The PDOS analysis was employed to investigate orbital interactions between the *OCHO intermediate and PSA@Mo_2CO_2 (where PSA represents Al, Si, Sn, and Pb) to understand the bonding between PSA (Al, Si, Sn, and Pb) and *OCHO. The presence of two oxygen and one carbon atom shows more and less intense electronic states, respectively. As shown in Fig. 7(a).

View Article Online
DOI: 10.1039/D6NA00397D

The Al valence p-orbital electronic state, present far away from the Fermi level, shows less electron presence. The ineffective overlap between Al-p and O-p leads to the weaker *OCHO intermediate adsorption on Al@Mo_2CO_2. The Bader charge and CDD show that Al@Mo_2CO_2 has the most positive Bader charge and leads to a weaker adsorption intermediate *OCHO (Fig. 7(b)). On the other hand, Fig. 7(c) shows stronger p-p hybridization between Si-p and O-p on the valence-band side. Hence, the bond length between Si ─ O is the shortest (1.64 Å), leading to the strong bonding between Si and O.

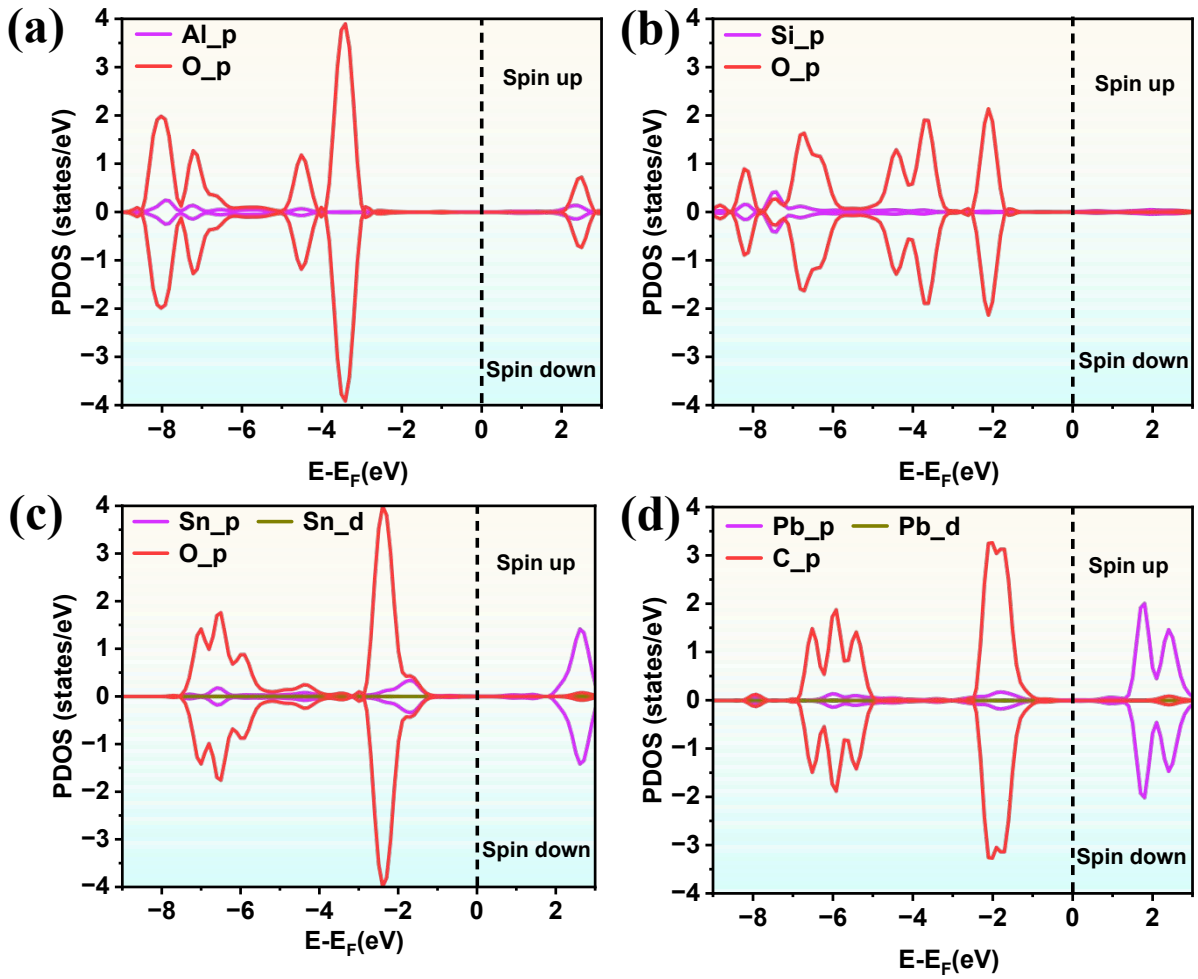

Fig. 7(a-d). Orbital interaction between PSA(Al, Si, Sn, and Pb) and *OCHO intermediate. The black short dash line at 0 eV represents the Fermi level.

View Article Online
DOI: 10.1039/D6NA00397D

In addition, CDD (Fig. 3) shows a higher charge-transfer from Si to O of *OCHO. The overlap between Sn p-orbital and O p-orbital hybridized near Fermi ($E-E_F = -1.70$ eV) shows p-p hybridization and moderate bonding. Whereas, in the case of Pb (Fig. 7(d)), the peak of valence p-orbital is far from the Fermi level at -1.80 eV, and intensity is also lower compared to the Sn p-orbital, which leads to weaker adsorption of the *OCHO intermediate. The bond length of Sn – O (2.26 Å) is lower compared to Pb – O (2.43 Å). This aligns with p-p hybridization and leads to moderate adsorption of *OCHO intermediate on $Sn@Mo_2CO_2$ and weaker adsorption on $Pb@Mo_2CO_2$. The best active $Sn@Mo_2CO_2$ catalyst stability is evaluated by using *ab initio* molecular dynamics simulations. The total energy obtained from the AIMD simulations is shown in Fig. S2 and exhibits small fluctuations without causing a rise in the catalyst's energy under dynamical conditions at 300K for 10 ps. This shows that $Sn@Mo_2CO_2$ remains stable at ambient conditions.

4. Conclusion

In this work, 23 $PSA@Mo_2CO_2$ and bare Mo_2CO_2 catalysts for electrochemical CRR were investigated using density functional theory. The binding and cohesive energy results suggest that, among 23 catalysts, 9 $PSA@Mo_2CO_2$ are the most stable catalysts. Side-on and end-on adsorption of CO_2 on $PSA@Mo_2CO_2$ predominantly results in linear geometries after energy minimization. Based on CO_2 adsorption and activation on Mo_2CO_2, PSA (Al, Si, In, Sn, and Pb) were screened, and PDOS analysis shows they exhibit metallic-like behavior. The Gibbs free energy diagram shows that the formation of *OCHO on $PSA@Mo_2CO_2$ is the potential-determining step, except for Si. The Gibbs free energy change for the potential-determining step is found to be in the order of $Sn@Mo_2CO_2 < Pb@Mo_2CO_2 < Al@Mo_2CO_2 < Mo_2CO_2$. Remarkably, $Sn@Mo_2CO_2$ is the most efficient catalyst with a low U_L value of −0.58 V, due to its optimal interaction with *OCHO, and

View Article Online
DOI: 10.1039/D6NA00397D

is also located at the top of the volcano plot. Interestingly, the Bader charge and CDD analyses show that Sn@Mo_2CO_2 exhibits a unique charge of –0.01 e on Sn, indicating that a higher charge is transferred from Mo_2CO_2 to Sn and then from Sn to *OCHO to maintain the neutral state. Hence, Sn acts as a mediator between Mo_2CO_2 and *OCHO, facilitating effective charge transfer. Additionally, Sn@Mo_2CO_2 shows the best selectivity toward CRR and inhibits HER. For better performance, the optimal p-p orbital overlap is essential. Furthermore, Sn@Mo_2CO_2 is thermally stable and may serve as an efficient catalyst for the formation of HCOOH from CO_2. This study provides orbital-based approaches for understanding catalytic behavior. Further, fine-tuning of the electronic properties of Mo_2CO_2 will help effectively convert CO_2 into value-added products.

View Article Online
DOI: 10.1039/D6NA00397D

Author contributions: CRediT

Anshul Gupta: Conceptualization, Methodology, Software, Data Curation, Investigation, Formal analysis, Writing original draft.

Shanmugam Ramasamy: Supervision, Validation, Resources, Funding acquisition, Review, and Editing.

Declaration of competing interests

The author declares no financial or personal relationship with other people or organizations that could influence or bias their work.

Acknowledgment

AG is thankful to VIT management for the fellowship and CO_2RGTC for the computing facilities. RS acknowledges VIT for the SEED grant support with the reference number RGEMS/SG20220030. We thank the HPC facility for the computational resources under DST-FIST grant number SR/FST/MS-II/2023/139(C).

References

1 S. C. Peter, *American Chemical Society*, 2018, preprint, DOI: 10.1021/acsenergylett.8b00878.

2 Y. Zhou, H. Cao, Z. An, M. Li, Y. Huo, J. Jiang, J. Xie and M. He, *Appl. Surf. Sci.*, DOI:10.1016/j.apsusc.2023.156492.

3 A. S. Agarwal, Y. Zhai, D. Hill and N. Sridhar, *ChemSusChem*, 2011, **4**, 1301–1310.

View Article Online
DOI: 10.1039/D6NA00397D

4 Q. Cheng, M. Huang, L. Xiao, S. Mou, X. Zhao, Y. Xie, G. Jiang, X. Jiang and F. Dong, *ACS Catal.*, 2023, **13**, 4021–4029.

5 Y. Linghu, T. Tong, C. Li and C. Wu, *Appl. Surf. Sci.*, DOI:10.1016/j.apsusc.2022.153001.

6 S. Emken, G. Di Liberto and G. Pacchioni, *Electrochim. Acta*, DOI:10.1016/j.electacta.2024.144714.

7 L. Liu, H. Akhoundzadeh, M. Li and H. Huang, *John Wiley and Sons Inc*, 2023, preprint, DOI: 10.1002/smtd.202300482.

8 D. N. Sredojević, I. Vukoje, Đ. Trpkov and E. N. Brothers, *Physical Chemistry Chemical Physics*, 2024, **26**, 8356–8365.

9 G. Xing, S. Liu and J. yao Liu, *Int. J. Hydrogen Energy*, 2023, **48**, 3486–3494.

10 Y. Shao, Q. Yuan and J. Zhou, *Small*, DOI:10.1002/smll.202303446.

11 M. Li, H. Wang, W. Luo, P. C. Sherrell, J. Chen and J. Yang, *Wiley-VCH Verlag*, 2020, preprint, DOI: 10.1002/adma.202001848.

12 A. Vasileff, C. Xu, Y. Jiao, Y. Zheng and S. Z. Qiao, *Elsevier Inc*, 2018, preprint, DOI: 10.1016/j.chempr.2018.05.001.

13 Y. Cai, J. Fu, Y. Zhou, Y. C. Chang, Q. Min, J. J. Zhu, Y. Lin and W. Zhu, *Nat. Commun.*, DOI:10.1038/s41467-020-20769-x.

14 Z. Wang, L. Sun, W. Li, J. Qin, Y. Li and Y. Wang, *Mater. Today Commun.*, DOI:10.1016/j.mtcomm.2025.113505.

15 S. Wang, L. Li, K. San Hui, F. Bin, W. Zhou, X. Fan, E. Zalnezhad, J. Li and K. N. Hui, *Adv. Eng. Mater.*, DOI:10.1002/adem.202100405.

16 P. Komen, S. Suthirakun, A. Plucksacholatarn, S. Kuboon, K. Faungnawakij and A. Junkaew, *J. Colloid Interface Sci.*, 2025, **679**, 1026–1035.

17 Z. Sun, R. Li, Q. Xi, F. Xie, X. Jian, X. Gao, H. Li, Z. Yu, J. Liu, X. Zhang, Y. Wang, Y. Wang, X. Yue and C. Fan, *Physical Chemistry Chemical Physics*, DOI:10.1039/d3cp00779k.

18 Y. Yang, J. Li, C. Zhang, Z. Yang, P. Sun, S. Liu and Q. Cao, *Journal of Physical Chemistry C*, 2022, **126**, 4338–4346.

19 P. Sikam, K. Takahashi, T. Roongcharoen, T. Jitwatanasirikul, C. Chitpakdee, K. Faungnawakij and S. Namuangruk, *Appl. Surf. Sci.*, DOI:10.1016/j.apsusc.2021.149380.

20 Z. Lu, P. Lv, Z. Yang, S. Li, D. Ma and R. Wu, *Physical Chemistry Chemical Physics*, 2017, **19**, 16795–16805.

View Article Online
DOI: 10.1039/D6NA00397D

21 H. Da Ren, Z. L. Lang, H. Q. Tan, Y. H. Wang and Y. G. Li, *Journal of Physical Chemistry C*, 2024, **128**, 6702–6710.

22 H. P. Zhang, R. Zhang, C. Sun, Y. Jiao and Y. Zhang, *Nanoscale*, 2021, **13**, 20541–20549.

23 A. Athawale, B. M. Abraham, M. V. Jyothirmai and J. K. Singh, *The Journal of Physical Chemistry C*, 2023, **127**, 24542–24551.

24 Y. Gogotsi and B. Anasori, *American Chemical Society*, 2019, preprint, DOI: 10.1021/acsnano.9b06394.

25 S. Baskaran and J. Jung, *Appl. Surf. Sci.*, DOI:10.1016/j.apsusc.2022.153339.

26 B. Mohanty, B. K. Jena and S. Basu, *ACS Omega*, 2020, **5**, 1287–1295.

27 B. R. Anne, J. Kundu, M. K. Kabiraz, J. Kim, D. Cho and S. Il Choi, *John Wiley and Sons Inc*, 2023, preprint, DOI: 10.1002/adfm.202306100.

28 X. Zhan, C. Si, J. Zhou and Z. Sun, *Royal Society of Chemistry*, 2020, preprint, DOI: 10.1039/c9nh00571d.

29 X. Sun, L. Sun, G. Li, Y. Tuo, C. Ye, J. Yang, J. Low, X. Yu, J. H. Bitter, Y. Lei, D. Wang and Y. Li, *Angew. Chem. Int. Ed.*, DOI:10.1002/anie.202207677.

30 J. Yu, J. Li, C. Y. Xu, Q. Li, Q. Liu, J. Liu, R. Chen, J. Zhu and J. Wang, *Nano Energy*, DOI:10.1016/j.nanoen.2022.107266.

31 J. Guo, F. Yu, Y. You, J. Zhan and L. H. Zhang, *Appl. Catal. B*, DOI:10.1016/j.apcatb.2024.124160.

32 Y. Li, D. Gao, C. Tang, Z. Guo, N. Miao, B. Sa, J. Zhou and Z. Sun, *J. Colloid Interface Sci.*, 2024, **658**, 114–126.

33 C. Zhang, W. Chu, C. Chen and W. Sun, *Catal. Today*, 2024, 114649.

34 G. Chen, M. Buraschi, R. Al-Heidous, S. Bonakala, F. El-Mellouhi and C. S. Cucinotta, *Journal of Physical Chemistry C*, DOI:10.1021/acs.jpcc.4c02283.

35 H. Liu, D. Liu, Z. Yu, H. Bai and H. Pan, *J. Colloid Interface Sci.*, 2025, **683**, 170–177.

36 R. K. Mishra, G. J. Choi, H. J. Choi, J. Singh, S. H. Lee and J. S. Gwag, *J. Alloys Compd.*, DOI:10.1016/j.jallcom.2022.166018.

37 Y. Jiang, S. Li, F. Zhang, W. Zheng, L. Zhao and Q. Feng, *Catal. Commun.*, DOI:10.1016/j.catcom.2021.106325.

38 X. Yang, J. Cheng, X. Yang, Y. Xu, W. Sun and J. Zhou, *Chemical Engineering Journal*, DOI:10.1016/j.cej.2021.134171.

39 Q. Liu, H. Cheng, X. Wang and P. Qian, *Physical Chemistry Chemical Physics*, 2023, **25**, 5056–5065.

View Article Online
DOI: 10.1039/D6NA00397D

40 R. Meshkian, L. Å. Näslund, J. Halim, J. Lu, M. W. Barsoum and J. Rosen, *Scr. Mater.*, 2015, **108**, 147–150.

41 M. Khazaei, M. Arai, T. Sasaki, M. Estili and Y. Sakka, *Physical Chemistry Chemical Physics*, 2014, **16**, 7841–7849.

42 C. Cheng, X. Zhang, M. Wang, S. Wang and Z. Yang, *Physical Chemistry Chemical Physics*, 2018, **20**, 3504–3513.

43 K. Kotmool, T. Kaewmaraya, T. Hussain, R. Ahuja, W. Luo and T. Bovornratanaraks, *Physical Chemistry Chemical Physics*, 2022, **24**, 17862–17869.

44 J. Gan, F. Li, Y. Tang and Q. Tang, *ChemSusChem*, 2020, **13**, 6005–6015.

45 R. Morales-Salvador, J. D. Gouveia, Á. Morales-García, F. Viñes, J. R. B. Gomes and F. Illas, *ACS Catal.*, 2021, **11**, 11248–11255.

46 P. Giannozzi, S. Baroni, N. Bonini, M. Calandra, R. Car, C. Cavazzoni, D. Ceresoli, G. L. Chiarotti, M. Cococcioni, I. Dabo, A. Dal Corso, S. de Gironcoli, S. Fabris, G. Fratesi, R. Gebauer, U. Gerstmann, C. Gougoussis, A. Kokalj, M. Lazzeri, L. Martin-Samos, N. Marzari, F. Mauri, R. Mazzarello, S. Paolini, A. Pasquarello, L. Paulatto, C. Sbraccia, S. Scandolo, G. Sclauzero, A. P. Seitsonen, A. Smogunov, P. Umari and R. M. Wentzcovitch, *Journal of Physics: Condensed Matter*, 2009, **21**, 395502.

47 J. P. Perdew, K. Burke and M. Ernzerhof, *Phys. Rev. Lett.*, 1996, **77**, 3865–3868.

48 J. P. Perdew, K. Burke and M. Ernzerhof, *Phys. Rev. Lett.*, 1998, **80**, 891.

49 S. Grimme, *J. Comput. Chem.*, 2006, **27**, 1787–1799.

50 K. Momma and F. Izumi, *J. Appl. Crystallogr.*, 2011, **44**, 1272–1276.

51 H. Shen, T. Wang, H. Jiang, P. Zhao, Z. Chen, Y. Feng, Y. Cao, Y. Guo, Q. Zhang and H. Zhang, *Appl. Catal. B*, 2023, **339**, 123140.

52 J. K. Nørskov, T. Bligaard, A. Logadottir, J. R. Kitchin, J. G. Chen, S. Pandelov and U. Stimming, *J. Electrochem. Soc.*, 2005, **152**, J23.

53 S. Wang, L. Li, J. Li, C. Yuan, Y. Kang, K. S. Hui, J. Zhang, F. Bin, X. Fan, F. Chen and K. N. Hui, *Journal of Physical Chemistry C*, 2021, **125**, 7155–7165.

54 S. Zhou, W. Pei, J. Zhao and A. Du, *Nanoscale*, 2019, **11**, 7734–7743.

55 NIST Chemistry WebBook, https://webbook.nist.gov/chemistry/, (accessed 20 October 2025).

56 J. K. Nørskov, J. Rossmeisl, A. Logadottir, L. Lindqvist, J. R. Kitchin, T. Bligaard and H. Jónsson, *Journal of Physical Chemistry B*, 2004, **108**, 17886–17892.

57 S. Cao, Y. Hu, C. Yang, J. Li, H. Chen, S. Wei, S. Liu, Z. Wang, D. Sun and X. Lu, *Journal of CO2 Utilization*, DOI:10.1016/j.jcou.2022.102074.

View Article Online
DOI: 10.1039/D6NA00397D

58 H. Zhou, Z. Chen, E. Kountoupi, A. Tsoukalou, P. M. Abdala, P. Florian, A. Fedorov and C. R. Müller, *Nat. Commun.*, DOI:10.1038/s41467-021-25784-0.

59 B. Huang, N. Li, W. J. Ong and N. Zhou, *J. Mater. Chem. A Mater.*, 2019, **7**, 27620–27631.

60 S. A. Khan, G. Rehman, I. Ahmad, M. Maqbool, C. Franchini and B. Amin, *Chem. Phys. Lett.*, DOI:10.1016/j.cplett.2019.136614.

61 Y. W. Sun and J. Y. Liu, *Physical Chemistry Chemical Physics*, 2023, **25**, 4773–4779.

62 B. H. Lee, J. Park, A. Kumar, S. Choi, D. H. Kim and S. Y. Lee, *Mater. Today Commun.*, DOI:10.1016/j.mtcomm.2022.104809.

63 C. Wu, X. Li, J. Lu, Z. Ye, J. Zhang, T. Zhou, R. Sun, L. Chen, B. Lu and X. Pan, *Appl. Phys. Lett.*, DOI:10.1063/1.4818728.

64 Z. Chen, J. W. Wang, Y. Song and X. Zuo, *AIP Adv.*, DOI:10.1063/1.4998280.

65 C. J. Lombard, C. G. C. E. van Sittert, J. N. Mugo, C. Perry and D. J. Willock, *Physical Chemistry Chemical Physics*, 2023, **25**, 6121–6130.

66 Z. Wei, Y. Li, P. Li, L. Pan, W. Li, X. Hu and Y. Gu, *RSC Adv.*, 2024, **14**, 6262–6269.

67 J. Zhao, N. Ma, T. Wang, N. Li, Y. Wang and J. Fan, *J. Mater. Chem. A Mater.*, 2022, **10**, 21611–21621.

68 S. Cao, Y. Liu, Y. Hu, J. Li, C. Yang, Z. Chen, Z. Wang, S. Wei, S. Liu and X. Lu, *J. Colloid Interface Sci.*, 2023, **642**, 273–282.

69 S. Liu, Z. Zhou, J. Chen, Y. Fu and C. Cai, *Appl. Surf. Sci.*, DOI:10.1016/j.apsusc.2022.155645.

70 X. Wang, H. Qin, Y. Chen and J. Hu, *Journal of Physical Chemistry C*, 2014, **118**, 28548–28561.

71 X. Mao, G. Kour, L. Zhang, T. He, S. Wang, C. Yan, Z. Zhu and A. Du, *Catal. Sci. Technol.*, 2019, **9**, 6800–6807.

72 L. I. Bendavid and E. A. Carter, *Journal of Physical Chemistry C*, 2013, **117**, 26048–26059.

73 F. Li and Q. Tang, *Nanoscale*, 2019, **11**, 18769–18778.

74 J. T. Feaster, C. Shi, E. R. Cave, T. Hatsukade, D. N. Abram, K. P. Kuhl, C. Hahn, J. K. Nørskov and T. F. Jaramillo, *ACS Catal.*, 2017, **7**, 4822–4827.

75 J. Quílez-Bermejo and J. Herranz, *J. Mater. Chem. A Mater.*, DOI:10.1039/d5ta03854e.

76 Z. Yang, F. E. Oropeza and K. H. L. Zhang, *APL Mater.*, DOI:10.1063/5.0004194.

View Article Online
DOI: 10.1039/D6NA00397D

77 S. Y. Wu, T. C. Chuang and H. T. Chen, *Appl. Surf. Sci.*, DOI:10.1016/j.apsusc.2024.161523.

78 A. J. Medford, A. Vojvodic, J. S. Hummelshøj, J. Voss, F. Abild-Pedersen, F. Studt, T. Bligaard, A. Nilsson and J. K. Nørskov, *J. Catal.*, 2015, **328**, 36–42.

79 S. H. Zhou, W. Wei, X. Cai, D. D. Ma, S. M. Wang, X. Li and Q. L. Zhu, *Adv. Funct. Mater.*, DOI:10.1002/adfm.202311422.

View Article Online
DOI: 10.1039/D6NA00397D

Data availability statements

The supporting data are provided in the Supplementary Information.